Estimating aboveground biomass using Pléiades satellite image in a karst watershed of Guizhou Province, Southwestern China

GUO Yin-ming[1,2,3] http://orcid.org/0000-0003-1425-6413; ✉e-mail: yinmingguo1220@163.com

NI Jian[1,2,4]* http://orcid.org/0000-0001-5411-7050; e-mail: nijian@zjnu.edu.cn

LIU Li-bin[1,2,3,4] http://orcid.org/0000-0003-3902-9954; e-mail: liulibin@zjnu.cn

WU Yang-yang[1,2,3] http://orcid.org/0000-0003-4222-3117; e-mail: wuyang2468@hotmail.com

GUO Chun-zi[1,2,3] http://orcid.org/0000-0002-8004-4147; e-mail: guochunzi@mail.gyig.ac.cn

XU Xin[1,2,3] http://orcid.org/0000-0003-1411-0406; e-mail: xuxin@mail.gyig.ac.cn

ZHONG Qiao-lian[1,2,3] http://orcid.org/0000-0002-2120-5086; e-mail: zhongqiaolian@mail.gyig.ac.cn

Corresponding author

1 State Key Laboratory of Environmental Geochemistry, Institute of Geochemistry, Chinese Academy of Sciences, Guiyang 550081, China

2 Puding Karst Ecosystem Research Station, Chinese Academy of Sciences, Puding 562100, China

3 University of Chinese Academy of Sciences, Beijing 100049, China

4 College of Chemistry and Life Sciences, Zhejiang Normal University, Jinhua 321004, China

Abstract: Biomass in karst terrain has rarely been measured because the steep mountainous limestone terrain has limited the ability to sample woody plants. Satellite observation, especially at high spatial resolution, is an important surrogate for the quantification of the biomass of karst forests and shrublands. In this study, an artificial neural network (ANN) model was built using Pléiades satellite imagery and field biomass measurements to estimate the aboveground biomass (AGB) in the Houzhai River Watershed, which is a typical plateau karst basin in Central Guizhou Province, Southwestern China. A back-propagation ANN model was also developed. Seven vegetation indices, two spectral bands of Pléiades imagery, one geomorphological parameter, and land use/land cover were selected as model inputs. AGB was chosen as an output. The AGB estimated by the allometric functions in 78 quadrats was utilized as training data (54 quadrats, 70%), validation data (12 quadrats, 15%), and testing data (12 quadrats, 15%). Data-model comparison showed that the ANN model performed well with an absolute root mean square error of 11.85 t/ha, which was 9.88% of the average AGB. Based on the newly developed ANN model, an AGB map of the Houzhai River Watershed was produced. The average predicted AGB of the secondary evergreen and deciduous broadleaved mixed forest, which is the dominant forest type in the watershed, was 120.57 t/ha. The average AGBs of the large distributed shrubland, tussock, and farmland were 38.27, 9.76, and 11.69 t/ha, respectively. The spatial distribution pattern of

the AGB estimated by the new ANN model in the karst basin was consistent with that of the field investigation. The model can be used to estimate the regional AGB of karst landscapes that are distributed widely over the Yun-Gui Plateau.

Introduction

Forests store large amounts of carbon and thus estimates of forest biomass are essential for investigating the carbon storage and cycle in terrestrial ecosystems at local, regional, and global scales (Drake et al. 2003; Main-Knorn et al. 2013). Estimates are also required for quantifying the carbon sequestration in forests (Temesgen et al. 2015). Traditional methods, which are based on field measurements, and new techniques, which are based on various remote sensing products (Anaya et al. 2009; Zhang et al. 2011; Fassnacht et al. 2014; Quan et al. 2017), are two common approaches to estimating aboveground biomass (AGB) quantitatively. The former cannot be applied to large spatial or multiple temporal scales because they are time consuming and costly. The latter can provide an effective means of achieving precise multi-temporal and multi-spatial estimates of AGB (Anaya et al. 2009; Shu et al. 2014).

Moderate- or low-resolution satellite images with low or no acquisition cost (Powell et al. 2010; Tian et al. 2012; Zolkos et al. 2013) are the most widely used and available sensor products. Radio detection and ranging (RADAR), light detection and ranging (LiDAR), hyperspectral imagery, and multiangular remote sensing data have also been successfully applied to AGB estimation, forest canopy cover and height, tree density, and land-cover studies (Sedano et al. 2008; Chopping et al. 2009, 2012; Stagakis et al. 2010; Laurin et al. 2014, 2016; Arrogante-Funes et al. 2017). Various kinds of vegetation indices (VIs) (Tian et al. 2012) can be calculated from plant reflectance and are related to AGB. The predictor data (sensor) type is the most important factor of accuracy of AGB estimates (Fassnacht et al. 2014). Numerous commercial satellites with very high resolution, such as IKONOS, QuickBird, WorldView-1, WorldView-2,

and Pléiades satellite imagery, have been successfully used to determine forest AGBs (Deng et al. 2014; Maack et al. 2015). Artificial neural networks (ANNs) can achieve a more accurate estimation of forest biomass than the commonly used methods of regression models (Xie et al. 2009; Pradhan et al. 2010; Vahedi et al. 2016).

Forests in mountainous areas are a key terrestrial ecosystem, but forest biomass is difficult to measure directly, even by using a remote-sensing approach. Relevant biomass estimates are therefore of great scientific significance in remote sensing data applications. Mountainous forests account for ca. 2/3 of the territorial area of China and approximately 90% of the total area (2.08×10^6 ha) of Chinese forests (Zhou et al. 2015), which influence the regional carbon budget considerably. The mountainous area of Southwestern China is one of the largest areas for forest growth and characterized by its unique geomorphology. This landform, which is typical of a carbonate bedrock, is characterized by an extremely slow soil formation from the underlying limestone and dolomite, with shallow, patchy soil and low water retention capacity (Liu et al. 2016a). Karst landscapes are continuously and broadly distributed in subtropical Guizhou. Quantifying AGB in this unique karst region is important for improving the accuracy of estimating Chinese AGB and for evaluating the role of karst ecosystems in the global carbon cycle. Numerous studies have been conducted on estimating forest AGB using all kinds of remote sensing data in other mountain forest ecosystems (Soenen et al. 2010; Clark et al. 2011; Brovkina et al. 2016; Ma et al. 2017). However, high habitat heterogeneity, high vegetation fragmentation, complex and irregular plant growth forms, and the steep and rocky karst mountains have limited our ability to sample woody plants. The AGBs of different vegetation types in such soluble, harsh, and fragile habitats are difficult to measure and have seldom been studied (Zhu et al. 1995; Yu et al. 2010; Du et al. 2010; Liu et al. 2013). Most of the studies were conducted in few forest quadrats and a small area of quadrats (Liu et al. 2009; Fan et al. 2015; Liu et al 2016a). Although field observation can reach acceptable levels of accuracy, they are inadequate for mapping the AGB distribution on a regional scale. Only a handful of studies on AGB mapping

have used moderate- or low-resolution satellite images (Caldwell et al. 2007; Zeng et al. 2007; Gao et al. 2013; Zhang et al. 2013, 2015), which cannot precisely estimate the forest biomass in mountainous and karst landscapes.

Therefore, the AGB in this special karst region, especially in secondary forests and degraded shrubland from human-induced rocky desertification (Jiang et al. 2014), should be accurately determined through very high-resolution (VHR) satellite imagery. Mountains in a karst region are tapered, which is unusual compared to the mountains in a non-karst region. This observation indicates that the slope of a karst tapered mountain is deep, typically between 20° and 40°. However, we have yet to determine whether VHR satellite images can reflect such a deep slope or whether the ANN method can precisely estimate karst forest and shrubland biomasses. In this study, a karst ANN model was built using a VHR Pléiades satellite imagery and by conducting field biomass measurements to estimate the AGB for all vegetation types in the Houzhai River Watershed, a typical plateau karst basin in Central Guizhou Province, Southwestern China. The amount and spatial distribution pattern of the AGB of karst forest and shrubland are further analyzed.

1 Study Area

The Houzhai River Watershed (26° 12′-26° 18′ N, 105° 40′-105° 49′ E; Figure 1) in Puding County, a typical and representative basin in the plateau-surface karst morphological region with an area of ca. 75 km², is located in Central Guizhou plateau, Southwestern China. Puding County has a subtropical humid monsoon climate, with mild summers and no chilly winters. The moderate climate and plentiful rainfall favor the growth of plants. The mean annual temperature in Puding weather station (26° 19′ N, 105° 45′ E, 1250 m, averaged between 1961 and 2013) is 15.2 °C, with temperatures of 5.2 °C and 23 °C in January and July, respectively. The mean annual precipitation is 1340.9 mm, with ca. 85% of rain falls in May to October. However, the mean annual sunshine is only 1189 h, and the sunshine percentage for the entire year is 26.3%.

The watershed is high in the southeast, with many cone peaks, depressions, and running underground rivers. By comparison, the watershed is low in the northwest and featured with plains, hills, and flowing ground rivers (Figures 1a, 1b). The elevation ranges from 1220 m to 1563 m with an average of 1312 m (Figure 1b), and the slope angle varies from 0° to 75° with an average of 11° (Figure 1c). A total of 142 visible peaks are found in the watershed. The bedrock is limestone and dolomite with thin gyp layers.

Black limestone soil in the hilly upper reaches, paddy soil in the middle plains and depressions, and yellow soil in the lowland lower reaches are the main soil types of this region (Figure 1d). The soils are shallow and have low total storage, but they are rich in organic carbon. The vegetation in this area is different from that of the typical evergreen broadleaved forest in non-karst subtropical regions (Wu 1980). The primary mixed evergreen and deciduous broad-leaved forest in the karst terrain was subjected to clearcutting in the 1950s. Secondary forests, including the mixed forest, evergreen broadleaved forest, deciduous broadleaved forest, and coniferous forest plantation, are common in hills, accounting for ca. 30% of the total watershed area. The forests on hill tops have few incidences of human disturbances. Degraded evergreen and deciduous shrublands and tussocks are found in middle parts and foothills. Rape-rice rotation is the main land use in the basin and depression, and maize is cultivated in middle parts and foothills (Liu et al. 2016a). The dominant tree species of the forests include *Platycarya strobilacea, Machilus cavaleriei, Quercus* spp.*, Lithocarpus* spp., and *Itea* spp. Shrubs, such as *Pyracantha fortuneana, Coriaria sinica, Rosa cymosa, Rhamnus parvifolia*, and *Zanthoxylum planispinum*, are also widely distributed.

2 Materials and Methods

2.1 Remote-sensing Data

VHR Pléiades satellite image data were acquired on 19 March 2013 under clear weather conditions. A panchromatic (pan) image at a geometric resolution of 0.5 m and a multispectral four-band (blue, green, red, and near-infrared
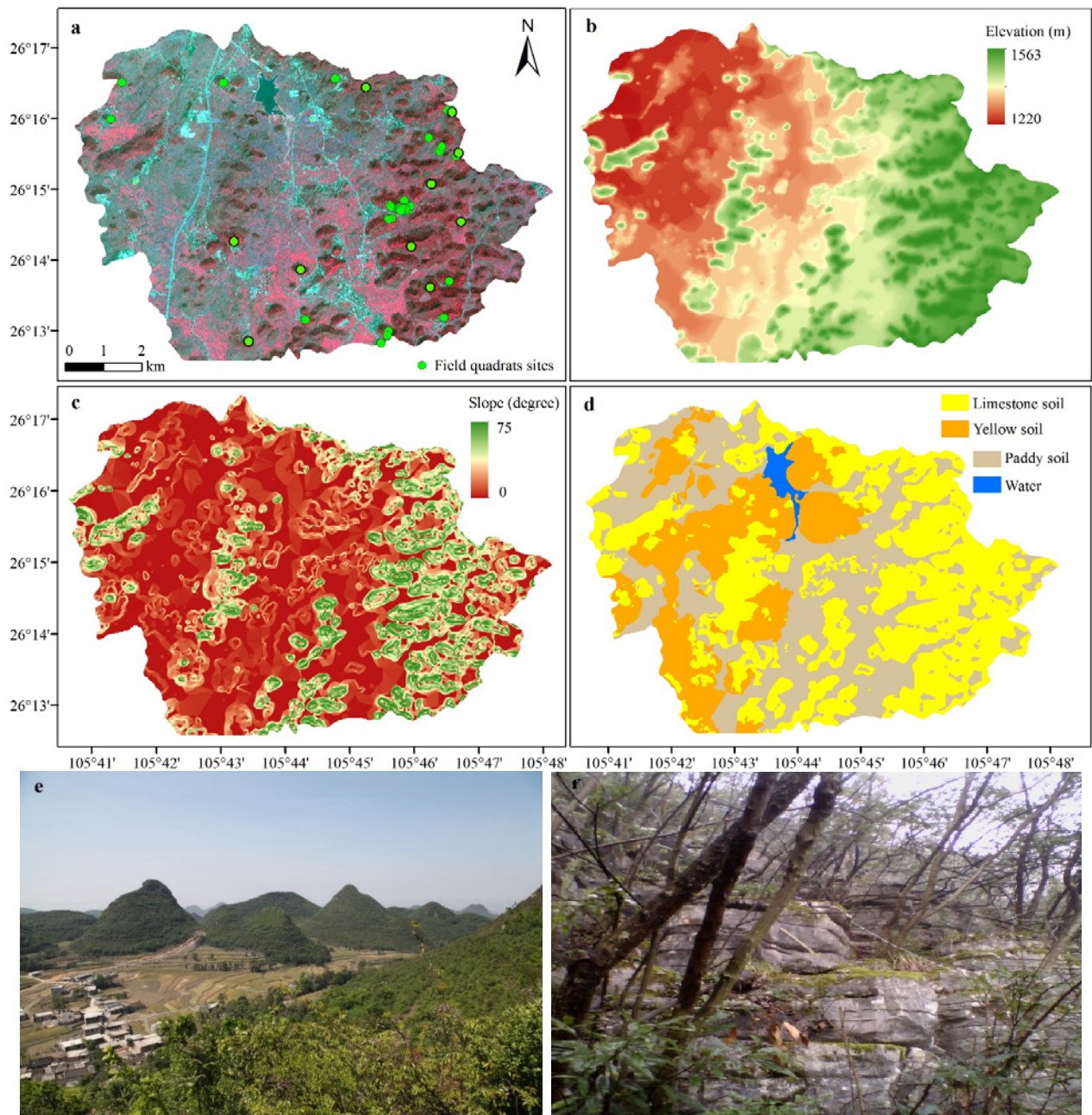
Figure 1 Location and field quadrat sites (green dot) (a), elevation (b), slope (c), spatial distribution of major soil types (d), physiognomy (e), and the general map (f) of the Houzhai River Watershed, Guizhou, China.

bands) image at a geometric resolution of 2 m were acquired. A digital elevation model (DEM) was created on the basis of SPOT-5 images at a geometric resolution of 10 m. The coordinate system of all image data was converted to Universal Transverse Mercator Zone 48N, World Geodetic System 1984.

Data pre-processing for the Pléiades imagery included several steps. First, we performed standard radiometric conversion from digital numbers to radiance using the sensor specific calibration coefficients provided in the images' metadata. Second, meaningful spectral reflectance signatures of the tree species' atmospheric correction was derived using the fast line-of-sight atmospheric analysis of the spectral hypercubes model. Finally, we applied geometric correction to minimize topographic and sensor geometry image distortions. All pre-processing activities were completed under the Environment for Visualizing

Images 5.3 and Geographical Information Systems 10.2. Details on data pre-processing can be found in other reports (Zhu et al. 2015; Clerici et al. 2016).

2.2 Land use/Land cover classification

The land use/land cover (LULC) of the Houzhai River Watershed was mapped from the satellite image by using object-based classification and the nearest neighbor classifier method in eCognition Developer 8.7 (Definiens Imaging). The segmentation in eCognition is a bottom-up region merging technique that involves the merging of small image objects into large ones with the scale parameter controlling the growth in heterogeneity between adjacent image objects. The input features of the training samples consist of a multi-dimensional feature space, and each sample has a class label (Zhu et al. 2015). Merging is stopped when the growth of an image object exceeds the threshold defined by the scale parameter (Laliberte et al. 2007). In our study, the segmentation parameters were continuously adjusted through repeated experiments and the comparison of the segmentation results. Parameter values 0.7, 0.3, 0.3, 0.7, and 30 were selected for the color index, shape index, smoothness index, compactness index, and scale parameter, respectively, because they produced the best visual effect, with singular entities outlining the objects of homogeneous appearance (Peña-Barragán et al. 2011). The

following 13 image attributes were used as input variables to train and construct the classifier: (1) 4 spectral attributes: mean values of 4 bands of Pléiades for each image object; (2) 2 vegetation attributes: Normalized Difference Vegetation Index (NDVI) and Enhanced Vegetation Index (EVI) for each image object; (3) 5 shape attributes: shape index, width, length/width, area, and density of each image object; and (4) 2 geomorphological attributes: DEM and slope angle for each image object.

In this study, six categories of LULC (Figure 2a) were classified on the basis of the GlobeLand30 classification system (Arsanjani et al. 2016) and the vegetation map of the Houzhai River Watershed (1:10,000) (Guo et al. 2013) (Figure 2b), including secondary forests (containing all forest types in the watershed), shrubland (containing all scrub types in the watershed), tussock (containing meadow and grass-forb community), farmland, construction land, and water. In addition, 380 GPS coordinates of the entire watershed were obtained for satellite data post-processing. Half of the collected GPS data points (190) was used in the classification process, whereas the other half was used for accuracy assessment by using the confusion matrix.

2.3 Training and Testing Data

Site-based biomass data include the training and testing data for remote sensing-based biomass
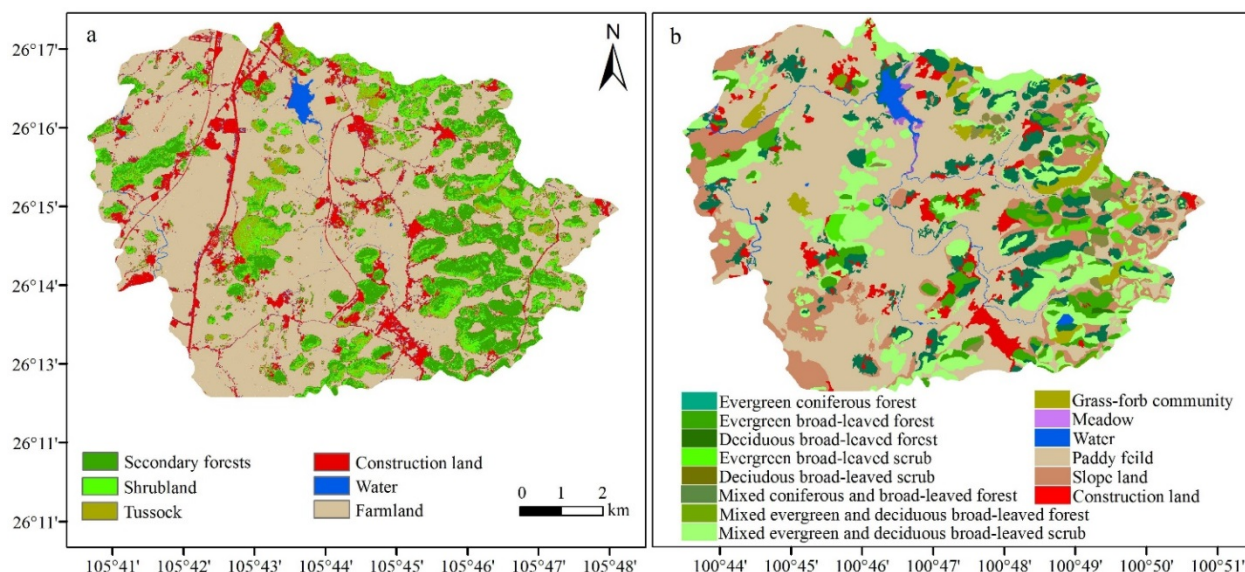
Figure 2 Land use/land cover (LULC) map from the Pléiades image data (a) and vegetation map of the Houzhai River Watershed.

reconstruction. A total of 78 vegetation quadrats (Figure 1a) were collected from 2007 to 2013 (Liu et al. 2009; Liu et al. 2013; Liu et al. 2016a; 2016b), as follows: 54 quadrats of secondary forests (each at 600–900 m²), 12 quadrats (100–200 m²) of shrubland, and 12 quadrats (100–200 m²) of tussock. Considering the large size of the study area and the representativeness of various forest patches, we divided 2 ha (horizontally-projected area) of the permanent monitoring quadrat of secondary forests (Liu et al. 2016b) in the watershed into 20 small quadrats (600–900 m²). The species; height (length for lianas and vines); diameter at breast height (DBH) for trees; basal diameter (BD) for shrubs, lianas, and vines; coverage of herbs; longitude; latitude; elevation; and the habitat information of each quadrat were recorded.

The AGBs of individual trees, shrubs, and lianas or vines in all the quadrats were estimated using species-specific and DBH- and BD-differentiated allometric functions, which were obtained by the standard tree method based on 15 dominant and common species in the watershed and surrounding regions (Zhu et al. 1995; Liu et al. 2009). The aboveground carbon (AGC) storage was calculated using the carbon concentrations (48.05%) averaged from the foliage and wood of 15 common species in the karst basin (Liu et al. 2013). The AGB and AGC of each quadrat were respectively summarized in terms of the AGB and AGC of all woody individuals, excluding herbs.

2.4 Calculation of Vegetation Indices

Vegetation indices (VIs) and spectral bands have been successfully used to estimate the AGB (Powell et al. 2010; Deng et al. 2014). Thirteen VIs were computed from the combinations of different spectral bands (Eckert et al. 2012; Clerici et al. 2016); four spectral bands of Pléiades imagery and four geomorphological variables that were derived from the DEM were screened on the basis of their relationships with the site biomass measurements. The longitude and latitude recorded in the vegetation survey were considered as the central points for calculating the mean values of all variables mentioned above in a 3 × 3 grid (6 m × 6 m) periphery. The variables without a significant correlation with AGB were removed for further analysis. Seven VIs, two spectral bands (blue band and red band), one geomorphological parameter (slope), and LULC were used as input parameters to build the ANN model. The vegetation index formulas (Wang et al. 2016) used in this study are listed in Table 1.

2.5 Building ANN model

Artificial intelligence modeling is a black box that consists of a series of complicated equations for calculating the outputs based on a given series of input values. ANNs can effectively deal with non-linear relationships (Menlik et al. 2010; Kumar et al. 2015) and learn from a sample set, which is called a training set, in a supervised or unsupervised learning process (Hassan et al. 2009). Each network consists of an input layer, an output layer, and one or more hidden layers that allow the network to learn relationships between input and output variables (Tiryaki et al. 2014).

Eleven variables, including ARVI, EVI, NDVI, DVI, GNDVI, RVI, SAVI, blue band, red band, slope, and LULC, were selected as inputs, and the AGB was chosen as output. A feed forward neural network that includes a back-propagation artificial neural network (BPANN) was used in this study. In this learning algorithm, an iterative gradient descent training procedure was used. Initial ANN weights were assigned randomly and adjusted

Table 1 Formulas of vegetation indices in this study

Index	Abbr.	Formula
Atmospherically Resistant Vegetation Index	ARVI	$ARVI = (R_{NIR} - (2 \times R_R - R_B))/(R_{NIR} + (2 \times R_R - R_B))$
Enhanced Vegetation Index	EVI	$EVI = 2.5 \times (R_{NIR} - R_R)/(1 + R_{NIR} + 6 \times R_R - 7.5 \times R_B)$
Normalized Difference Vegetation Index	NDVI	$NDVI = (R_{NIR} - R_R)/(R_{NIR} + R_R)$
Difference Vegetation Index	DVI	$DVI = R_{NIR} - R_R$
Green Normalized Difference Vegetation Index	GNDVI	$GNDVI = (R_{NIR} - R_G)/(R_{NIR} + R_G)$
Ratio Vegetation Index	RVI	$RVI = R_{NIR}/R_R$
Soil-Adjusted Vegetation Index	SAVI	$SAVI = 1.5 \times (R_{NIR} - R_R)/(R_{NIR} + R_R + 0.5)$

Note: R_R, R_G, R_B, and R_{NIR} represent the reflectance values of the red, green, blue, and near infrared bands of Pléiades imagery, respectively.

through a back-propagation mechanism. The weight adjustment process is repeated until the model output reaches an acceptable accuracy level (Zhu et al. 2015).

The input data were normalized between 0 and 1 because the 11 variables possessed different dimensions. The datasets were randomly partitioned into training data (70% of whole data), validation data (15%), and testing data (15%) during the BPANN development. The validation data were used to minimize overfitting, whereas the testing data were utilized to check the network performance and confirm its accuracy. The BPANN model was established with the MATLAB 2013a Neural Network Toolbox by using iterated cross-validation (CV) and stratified random sampling. The main tuning parameters for the network were continuously adjusted by comparing the root mean square error (RMSE) between the predicted and measured AGBs to determine the optimal network model. The learning rate and training accuracy were set to 0.01 and 0.001, respectively. The number of epochs was set to 6000, and the defaults in the MATLAB Neural Network Toolbox were used for the other parameters (Laliberte et al. 2007; Zhu et al. 2015). The newly developed BPANN model was extended to estimate the AGB of the entire Houzhai River Watershed based on the 11 selected variables. A final AGB map was produced using the GIS.

3 Results

3.1 Accuracy assessment

The accuracy of the LULC was evaluated using the confusion matrix based on the GPS coordinates and field dataset. The total accuracy of the LULC classification was 93.68%, and the kappa coefficient was 0.92, indicating that our interpretation and classification are adequate.

The R values in the training, validation, and testing data and in the entire dataset are greater than 0.95 (Figure 3), thereby suggesting that the designed model can explain more than 95% of the measured data. The comparison of the measured and predicted AGBs of the testing data indicates a low absolute RMSE of 11.85 t/ha, which is only 9.88% of the average AGB. The R and RMSE values imply that the established BPANN model exhibits
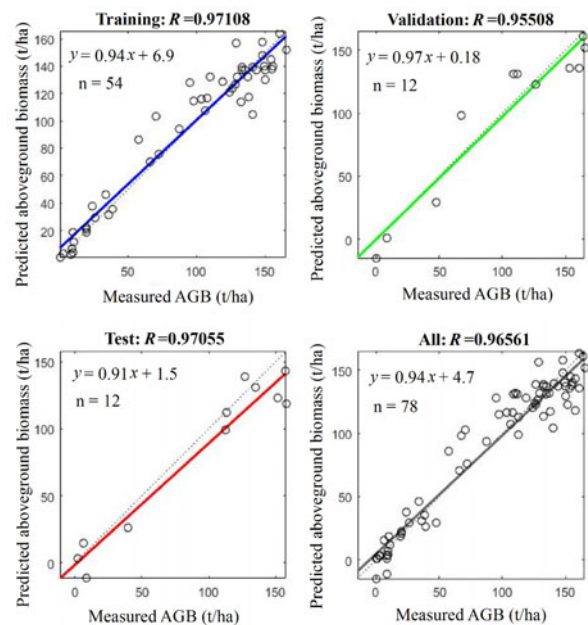

Figure 3 Relationship between the measured and predicted aboveground biomass by the BPANN model.

high accuracy and is fit for the estimation of AGB in the Houzhai River Watershed.

3.2 Vegetation Indices and measured AGB

The spatial distribution patterns of the seven VIs in the Houzhai River Watershed follow the same trends (Figures 4a-g). High VI values were mainly found in the east, southeast, and a small part of the west. These values are highly related to the distribution of secondary forests, shrubland, and tussock. Medium values of VIs were mostly distributed in the central and western parts of the watershed where most of the farmland is widespread. Low VI values were found in the construction land.

The 11 input variables and measured AGB in the field quadrats of the key vegetation types show that the highest VIs and AGB were found in secondary forests, whereas the lowest values were detected in tussock (Table 2). Results show that a positive correlation exists between AGB and the vegetation indices, but a negative correlation exists between AGB and the spectral bands. The slope angle of the secondary forest growth was steeper than those of shrubland and tussock growth because forests usually grow on hill tops, while the two other vegetation types thrive on foothills.
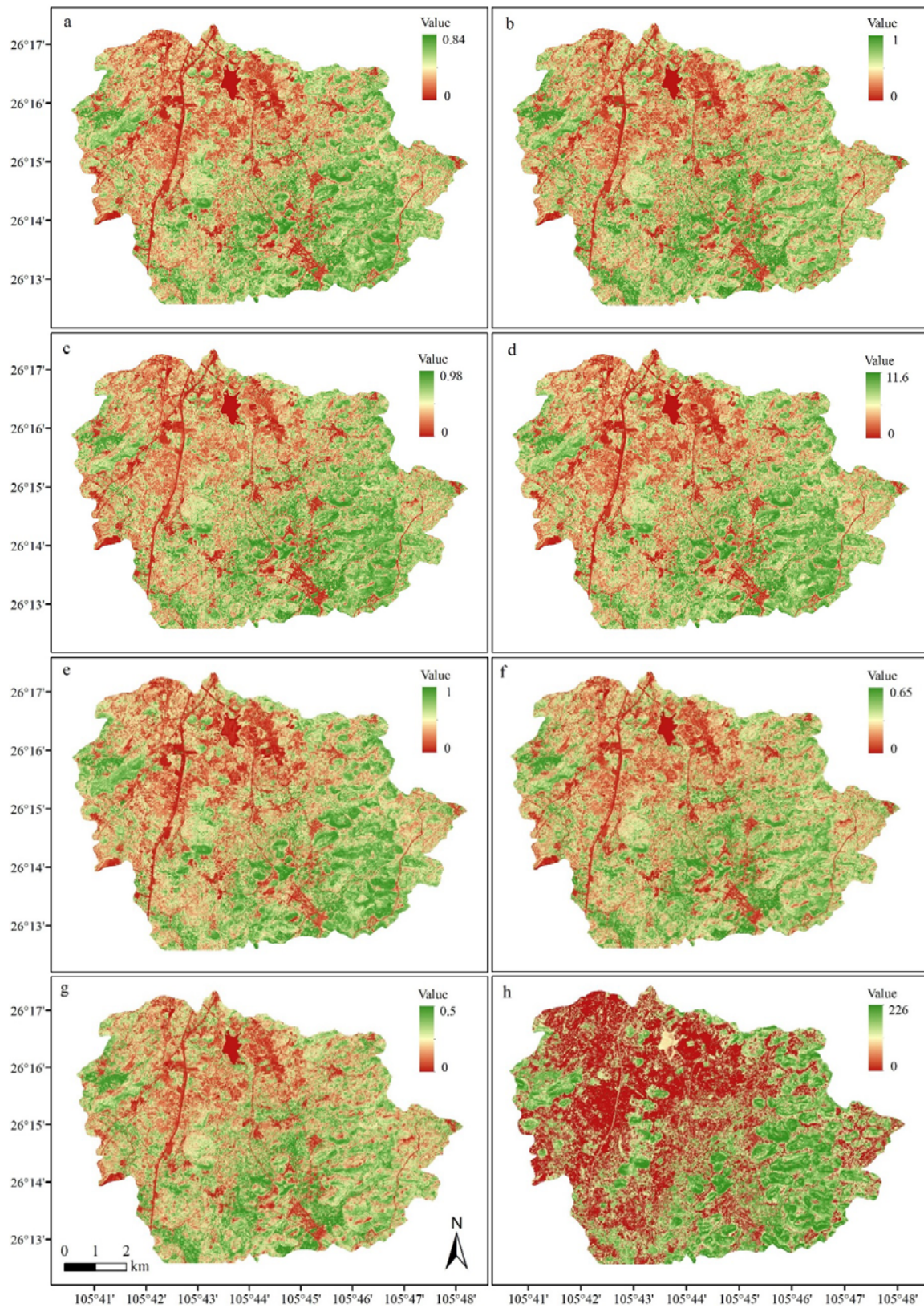
Figure 4 Spatial distribution patterns of vegetation indices and AGB (aboveground biomass) (t/ha) in Houzhai River Watershed: (a) Normalized Difference Vegetation Index, (b) Enhanced Vegetation Index, (c) Green Normalized Difference Vegetation Index, (d) Ratio Vegetation Index, (e) Atmospherically Resistant Vegetation Index, (f) Soil-Adjusted Vegetation Index, (g) Difference Vegetation Index, and (h) Aboveground biomass (t/ha).

3.3 Spatial Distribution Patterns of the Predicted AGB

The predicted AGB increases with the VIs. The spatial distribution of the predicted AGB (Figure 4h) exhibits the same trend as the VIs, but high values become increasingly evident at high elevations (Figure 1b). This pattern (Figure 4h) is also highly correlated with the patterns of vegetation and the LULC (Figure 2).

From each LULC type perspective, the spatial distribution patterns of the predicted AGB show the following: high AGB in secondary forests (Figure 5a) and shrubland (Figure 5b); and low AGB in the farmland and tussock (Figures 5c and 5d). Low AGBs in large areas are mainly found in the farmland (Figure 5d). Such patterns coincide with the distributions of elevation and soil types (Figures 1b, 1d). Table 3 shows details of the predicted ranges and averages of AGB of these four LULC types. R² is 0.9544 between the measured and predicted AGBs of the 78 quadrats (Figure 6). These findings indicate that the BPANN model exhibits high accuracy and is fit for estimating the

Table 2 Input variables and measured AGB (aboveground biomass) (mean ± standard error) of key vegetation types

Variable	SF	Shrubland	Tussock
ARVI	0.60 ± 0.01	0.52 ± 0.03	0.37 ± 0.06
EVI	0.34 ± 0.01	0.30 ± 0.02	0.21 ± 0.02
NDVI	0.62 ± 0.01	0.56 ± 0.02	0.45 ± 0.04
GNDVI	0.54 ± 0.01	0.50 ± 0.02	0.42 ± 0.04
SAVI	0.31 ± 0.01	0.28 ± 0.02	0.20 ± 0.02
RVI	4.52 ± 0.15	3.73 ± 0.21	2.73 ± 0.23
DVI	0.16 ± 0.01	0.14 ± 0.01	0.10 ± 0.01
Red band	447.53 ± 9.92	541.13 ± 37.47	621.45 ± 44.11
Blue band	405.24 ± 6.02	467.35 ± 21.11	479.55 ± 30.45
Slope angle	37.78 ± 1.56	16.30 ± 2.99	20.25 ± 3.97
AGB (t/ha)	128.47 ± 3.91	35.06 ± 3.04	8.77 ± 0.46
AGB range (t/ha)	57.94-157.85	19.53-57.95	6.1-10.61

Notes: SF = Secondary forests.

Table 3 Predicted AGB (aboveground biomass) in different LULC types

Vegetation types	Secondary forests	Shrubland	Tussock	Farmland
Biomass density (t/ha)	60 – 226	10 – 60	1 – 16	0 – 30
Mean AGB (t/ha)	120.57	38.27	9.76	11.69
Total AGB (t)	126760.60	25331.19	4252.08	52777.90
Area (ha)	1051.34	661.91	435.66	4514.79
Area ratio (%)	14.02	8.83	5.81	60.20

AGB in the Houzhai River Watershed.

The AGB pattern in the karst terrain is connected to the slope gradient (Figure 7). Low AGB is mainly found in a low slope angle of <15° (Figures 7a, 7b, with an average of 33.85 ± 13.21 t/ha), in which the farmland (rice and maize) is mainly distributed in the basin depression. A high slope angle (15°−35°) on hill tops exhibits high AGB (Figures 7c and 7d, with an average of 103.63 ± 33.56 t/ha), in which a large amount of secondary forests, shrubland, and tussock can be found. Even at a steep slope angle (35°−45° and above) at the cone peak, a high AGB distribution is observed (Figures 7e and 7f, with an average of 163.47 ± 16.26 t/ha). There, relatively well-protected forests can also be found. The consistency between the predicted AGB and the LULC indicates that the BPANN model provides satisfactory results for the prediction of AGB in a typical plateau karst basin.

In terms of model prediction, the total AGB in the Houzhai River Watershed is 0.215 Tg in a total area of 7500 ha, and the total AGC is 0.103 TgC. The AGBs of the secondary forests, shrubland, tussock, and farmland account for 59.00%, 11.79%, 1.98%, and 24.57% of the total AGB of this watershed, respectively.

4 Discussion

Given the large and unique area of the karst landscape in Southwestern China, the AGB and carbon storage in karst terrains should be precisely estimated to evaluate the role of karst ecosystems in regional and global carbon cycles. Traditional field measurement methods are accurate, but the obtained information may change quickly and become outdated because of the dynamic nature of forest environments (Temesgen et al. 2015). However, remote sensing technology may provide a supplement or a substitute with the advantages, such as large scale, integration, and dynamic estimation of forest biomass. In addition, it does not disrupt the harsh and fragile karst forest ecosystems and habitats.

Several remote sensing-based AGB or carbon storage studies have been conducted in these harsh and fragile habitats of Guizhou Province. Zheng et al. (2007) developed AGB estimation models for
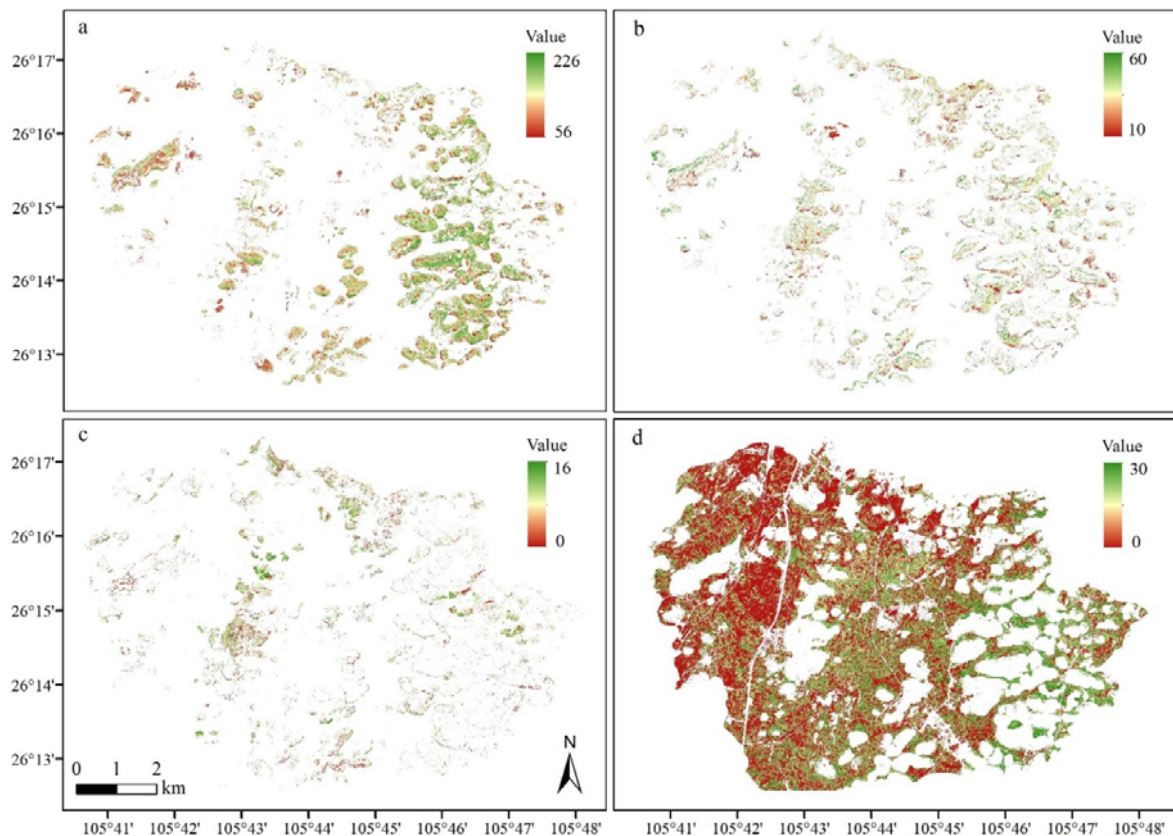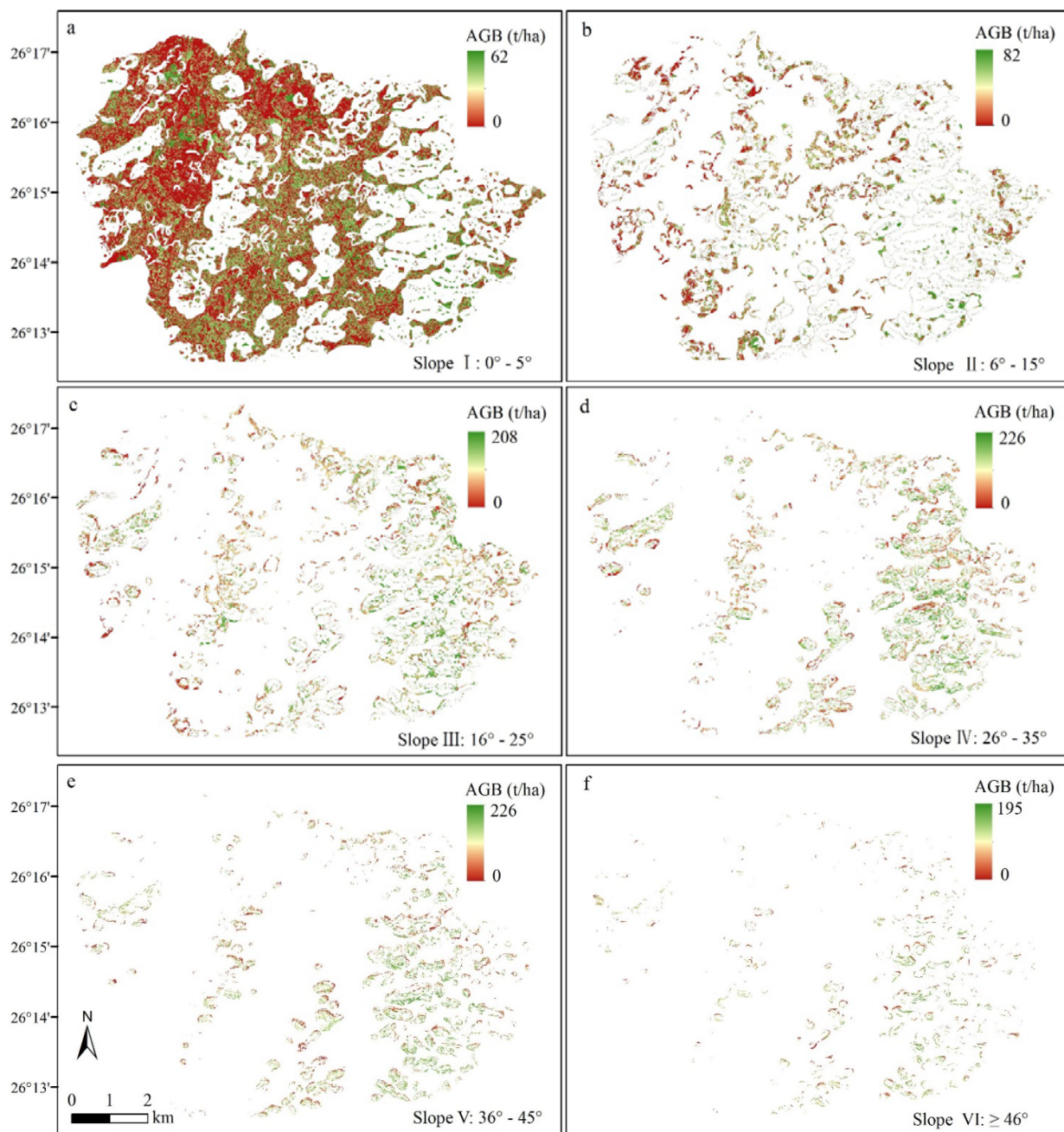
Figure 5 Spatial distribution patterns of AGB (aboveground biomass) in different LULC types in Houzhai River Watershed: (a) secondary forests, (b) shrubland, (c) tussock, and (d) farmland.
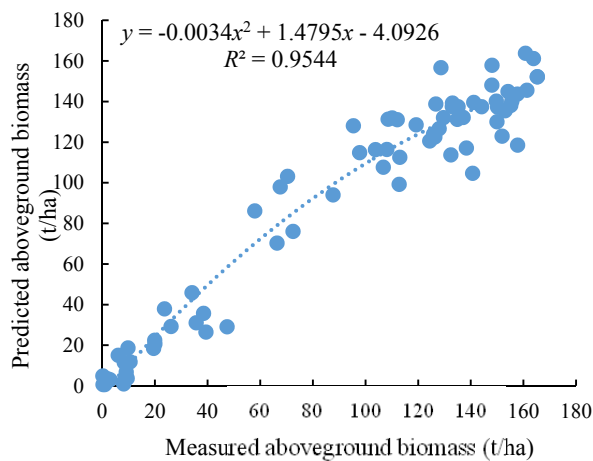
Figure 6 Correlation between the measured and predicted AGB (aboveground biomass) of the 78 quadrats in Houzhai River Watershed.

different forest types in Liping County, Southeastern Guizhou Province, which combine the LULC, ETM+ image (30 m × 30 m), and field forest inventory data. Their estimated forests AGB ranged from 40–200 t/ha, of which 64% have AGB levels between 90–180 t/ha. Zhang et al. (2015)

studied the spatial distribution patterns and historical carbon storage in Qinglong County, a typical karst canyon area in the Southwest of Guizhou, using Landsat TM and ETM+ image data (30 m × 30 m) of 1988, 1999, and 2009. In 2009, based on the proportion of AGC in the total carbon storage, their simulated average forests AGB was 133.31 t/ha, which is clearly higher than the average AGB of 87.62 ± 30.11 t/ha obtained from the field survey in the Qinglong Mengzhai Watershed from 2011 to 2013 (Fan et al. 2015) (a conversion factor of 48.05% was used to convert biomass to carbon content) (Liu et al. 2013). Gao et al. (2016) explored the effects of land use change on the carbon storage in Wujiang River in Guizhou from 2000 to 2010, using a model of integrated valuation of ecosystem services and trade-offs. They also analyzed the spatio-temporal variations of carbon storage based on the land use map from a Landsat TM/ETM image (30 m × 30 m). According to this research, the average AGBs of the forests (comprising evergreen coniferous forest, mixed coniferous and broad-leaved forest, and deciduous

Figure 7 Spatial distribution patterns of the predicted AGB (aboveground biomass) in different slope gradients in Houzhai River Watershed.

broad-leaved forest) and shrubland were 126.3 and 55.36 t/ha in 2010, respectively. Although regional variations exist in the AGB estimates, the estimates obtained in our study are lower than the previously mentioned data, especially the forest and shrubland biomass.

However, these previous studies were based on moderate- or low-resolution satellite image data. On one hand, previous research suggested that moderate- or low-resolution remote sensing

images, such as Landsat TM/ETM+ and MODIS dataset, cannot estimate AGBs in complex forests accurately because of the difficulty in linking coarse spatial-resolution data and field measurements or the failure to overcome problems associated with mixed pixels (Lu et al. 2006). Several studies also showed that Landsat TM satellite imagery can be beneficial for modeling the AGB in conifer forest areas, meadows, and pastures, but not for modeling the AGB in complex forest areas (Zheng

et al. 2004; Günlü et al. 2014; Barrachina et al. 2015). In addition, the limited spatial detail misses small-scale biomass variability. Meanwhile, the Pléiades satellite imagery with a very high resolution from tens of centimeters to a few meters provides an approach to this problem (Deng et al. 2014). Available literature has been systematically reviewed to identify the most common sensor types and prediction methods for biomass estimation, such as stepwise linear regression, support vector machines, random forest, Gaussian processes, and k-nearest neighbor. In addition, results have shown that a consensus on the best practices for biomass estimation has not been achieved yet, although the predictor data (sensor) type is the most important factor influencing the accuracy of biomass estimates (Fassnacht et al. 2014). Previous studies demonstrated that the mangrove forest information obtained from VHR images can improve the accuracy of AGB considerably (Zhu et al. 2015). These VHR satellite images, such as World View-1&2, Geo Eye-1, and Pléiades satellite imagery, coupled with the field quadrat dataset, provide a cost-effective framework for biomass and carbon stock estimation in complex secondary forest types at regional scales (Deng et al. 2014; Clerici et al. 2016). Consequently, moderate- or low-resolution satellite image data are not the best choice for estimating the AGB in mountainous and karst landscapes.

On the other hand, ANN models have no mathematical scaling parameters, but the architecture of each model can be determined according to the biomass variations based on the range of input nodes; thus, the correlation between outputs and targets is well understood and automatically assimilated into the connection weights of a network (Ozçelik et al. 2010). Previous research revealed that ANN model can predict AGB more accurately in natural forests than site-specific allometric equations can (Vahedi et al. 2016). In the estimation of the AGB of a typical grassland in Xilingol River Basin, Inner Mongolia, China, the ANN model provides a more precise estimation than the multiple linear regression (MLR) model (Xie et al. 2009). If ASTER satellite data combined with standwise forest inventory data are used, a more precise estimation of the biomass of boreal forests than a non-linear regression model can be achieved (Muukkonen et al. 2005). Therefore, our study could provide an easy, quick and accurate estimation of the AGB in such mountainous and karst landscapes.

Based on the newly developed BPANN model, the average AGB (120.57 t/ha) of secondary forests in this study is slightly lower than the AGB (137.7 t/ha) calculated from the field research of a 2-ha quadrat in the Houzhai River Watershed (Liu et al. 2016b). This is mainly because the 2-ha quadrat is located in the hill tops (1402-1512 m) with few incidences of human disturbances. Furthermore, the forest coverage and DBH and height of trees in the 2-ha quadrat were higher than other parts of the study area. Therefore, the average AGB from field survey should be higher than that obtained in our study. Meanwhile, the average AGB of secondary forests in this study was slightly higher than the AGB (65.4-115.2 t/ha, excluding the AGB of herbaceous layer) estimated by Liu et al. (2009) based on three small quadrats (each at 600 m2) in the surrounding area of the basin. This variation is mainly attributed to the differences in quadrat area calculation. The quadrat area in our study was calculated by horizontal projection according to the average slope of the quadrat. Liu et al. (2009) did not consider the horizontal projection and still used the small quadrat area of the original inclined hill slope; they only calculated the AGB of the tree layer and shrub layer, thereby resulting in a lower average AGB than that obtained in our study.

However, the averaged predicted AGB of the secondary forest (120.57 t/ha) and shrubland (38.27 t/ha) in this study are higher than the AGBs obtained from the field quadrat survey in the typical trough valley karst basin in Northern Guizhou (Zhong et al. 2014) and the canyon karst basin in Southwestern Guizhou (Fan et al. 2015). With a conversion factor of 48.05%, which was previously used to convert biomass to carbon content (Liu et al. 2013), the calculated AGBs of the secondary forest and shrubland of Zhong et al (2014) were 99.35 t/ha and 24.88 t/ha, respectively. The values reported by Fan et al. (2015) were 87.62 t/ha and 13.09 t/ha, respectively. The differences could be linked to the growth ages of the forests. The growth ages of the secondary forest are in the range of 63 years old to 94 years old in this study area (Liu et al. 2016), whereas those of the secondary forests are less than 50 years old, with lower DBH and trees in the latter

two areas (Zhong et al. 2014). Meanwhile, the average AGB of the secondary forest in our study is lower than that (168.02 t/ha) estimated by Zhu et al. (1995) in the peak-clump depression-type karst in Southern Guizhou. This result can be attributed to the fact that the cutting of the original karst forest in the former in the late 1950s completely modified the local habitat, thereby making the restoration of the original vegetation impossible for at least 50 years (Ni et al. 2015), while the latter was in the climax stage with higher DBH and tall trees. The results of our study are consistent with the previous studies.

Therefore, the combination of VHR Pléiades satellite imagery and the ANN model is the best for estimating AGB precisely in mountainous and karst landscapes. On the basis of the newly developed BPANN model, VHR Pléiades imagery, and local observational data, we can satisfactorily predict the AGB and AGC of forests, shrubland, tussock, and farmland in a typical plateau karst basin. This approach can be extended to the AGB estimation of basins with similar morphological characteristics in the southwestern karst region of China. However, the accuracy of the BPANN model in this study may be affected by the asymptotic saturation problems associated with the use of VIs for AGB estimation (Mutanga et al. 2012; Wang et al. 2017). LiDAR data can provide detailed vegetation structure measurements at discrete locations that cover the circular or elliptical footprints from a few centimeters to tens of meters in diameter (Montesano et al. 2013). Therefore, combining VHR satellite and LiDAR data is necessary to improve the accuracy of the estimation of AGB in forests in future studies.

5 Conclusion

On the basis of the proposed karst BPANN model and VHR Pléiades satellite imagery, we obtained the total AGB and the AGC in the Houzhai River Watershed of 0.215 and 0.103 Tg in a total area of 7500 ha, respectively. The AGBs of the secondary forests, shrubland, tussock, and farmland were 0.127, 0.025, 0.004, and 0.053 Tg, which accounted for 59.00%, 11.79%, 1.98%, and 24.57% of the total AGB of this watershed, respectively. The spatial distribution patterns and ranges of various vegetation AGBs predicted by the model were consistent with those obtained from field investigation. The biomass carbon of secondary forests is higher than those of shrubland, farmland, and tussock and often distributed in limestone soils at a high slope angle (>15°). Overall, the Pléiades image-based BPANN model provided satisfactory results for the prediction of AGB in the typical plateau karst basin. It can also be used to estimate the AGB of the karst landscapes distributed on the surface of the Yun-Gui Plateau on a regional scale.

Acknowledgements

References

Arrogante-Funes P, Novillo CJ, Romero-Calcerrada R, et al. (2017) Relationship between MRPV Model Parameters from MISRL2 Land Surface Product and Land Covers: A Case Study within Mainland Spain. International Journal of Geo-Information 6(11): 353. https://doi.org/10.3390/ijgi6110353

Arsanjani JJ, Tayyebi A, Vaz E (2016) GlobeLand30 as an alternative fine-scale global land cover map: Challenges, possibilities, and implications for developing countries. Habitat International 55: 25-31. https://doi.org/10.1016/j.habitatint.2016.2.003

Barrachina M, Cristóbal J, Tulla AF (2015) Estimating above-ground biomass on mountain meadows and pastures through remote sensing. International Journal of Applied Earth Observations and Geoinformation 38: 184-192. https://doi.org/10.1016/j.jag.2014.12.002

Brovkina O, Novotny J, Cienciala E, et al. (2017) Mapping forest aboveground biomass using airborne hyperspectral and LiDAR data in the mountainous conditions of Central Europe. Ecological Engineering 100: 219-230. https://doi.org/10.1016/j.ecoleng.2016.12.004

Caldwell IM, Maclaren VW, Chen JM, et al. (2007) An integrated assessment model of carbon sequestration benefits: A case study of Liping county, China. Journal of Environmental Management 85(3): 757-773. https://doi.org/10.1016/j.jenvman.2006.08.020

Clark ML, Roberts DA, Ewel JJ, et al. (2011) Estimation of tropical rain forest aboveground biomass with small-footprint lidar and hyperspectral sensors. Remote Sensing of Environment 115(11): 2931-2942. https://doi.org/10.1016/j.rse.2010.08.029

Clerici N, Rubiano K, Abd-Elrahman A, et al. (2016) Estimating aboveground biomass and carbon stocks in Periurban Andean

secondary forests using very high resolution imagery. Forests 7(7): 138. https://doi.org/10.3390/f7070138

Chopping M, Moisen GG, Su L, et al. (2009) Large area mapping of southwestern forest crown cover, canopy height, and biomass using the NASA Multiangle Imaging Spectro-Radiometer. Remote Sensing of Environment 112(5): 2051-2063. https://doi.org/10.1016/j.rse.2007.07.024

Chopping M, North M, Chen JQ, et al. (2012) Forest canopy cover and height from MISR in topographically complex Southwestern US landscapes assessed with high quality reference data. IEEE Journal of Selected Topics in Applied Earth Observations and Remote Sensing 5(1): 44-58. https://doi.org/10.1109/JSTARS.2012.2184270

Deng SQ, Katoh M, Guan QW, et al. (2014) Estimating forest aboveground biomass by combining ALOS PALSAR and WorldView-2 data: A case study at Purple Mountain National Park, Nanjing, China. Remote Sensing 6(9): 7878-7910. https://doi.org/10.3390/rs6097878

Drake JB, Knox RG, Dubayah RO, et al. (2003) Above-ground biomass estimation in closed canopy Neotropical forests using lidar remote sensing: factors affecting the generality of relationships. Global Ecology and Biogeography 12(2): 147-159. https://doi.org/10.1046/j.1466-822X.2003.00010.x

Du YX, Pan GX, Li LQ, et al. (2010) Partitioning of vegetation biomass, nutrient storage and cycling of degraded ecosystems from moutainous karst region, central Guizhou, China. Acta Ecologica Sinica 30(23): 6338-6347. (In Chinese)

Eckert, S (2012) Improved forest biomass and carbon estimations using texture measures from WorldView-2 satellite data. Remote Sensing 4(4): 810-829. https://doi.org/10.3390/rs4040810

Fan WJ, Rong L, Zhang ZQ (2015) Carbon distribution of main vegetation types of Mengzhai watershed in south China karst canyon area. Journal of Mountain Science 33(4): 457-464. (In Chinese) https://doi.org/10.16089/j.cnki.1008-2786.000057

Fassnacht FE, Hartig F, Latifi H, et al. (2014) Importance of sample size, data type and prediction method for remote sensing-based estimations of aboveground forest biomass. Remote Sensing of Environment 154: 102-114. https://doi.org/10.1016/j.rse. 2014.07.028

Gao HJ, Han HQ, Zhang CQ, et al. (2016) Eeffects of land use change on carbon storage in Wujiang river of Guizhou province from 2000 to 2010. Journal of Sichuan Agricultural University 34(1): 48-53. (In Chinese) https://doi.org/10.16036/j.issn.1000-2650.2016.01.009

Günlü A, Ercanli̇ I, BaşKent E Z, et al. (2014) Estimating aboveground biomass using Landsat TM imagery: a case study of Anatolian Crimean pine forests in Turkey. Annals of Forest Research 57(2): 289-298. https://doi.org/10.15287/afr.2014.278

Guo K, Liu CC, Qiao ZP, et al. (2013) Vegetation map of the Houzhai River Watershed in Puding County, Guizhou Province. Institute of Botany, the Chinese Academy of Sciences, Beijing, China. (In Chinese)

Hassan AM, Alrashdan A, Hayajneh MT, et al. (2009) Prediction of density, porosity and hardness in aluminum–copper-based composite materials using artificial neural network. Journal of Materials Processing Technology 209(2): 894-899. https://doi.org/10.1016/j.jmatprotec.2008.02.066

Jesúsa A, Emilio C, Alicia PO (2009) Aboveground biomass assessment in Colombia: A remote sensing approach. Forest Ecology and Management 257(4): 1237-1246. https://doi.org/10.1016/j.foreco.2008.11.016

Jiang ZC, Lian YQ, Qin XQ (2014) Rocky desertification in Southwest China: Impacts, causes, and restoration. Earth-Science Reviews 132(3): 1-12. https://doi.org/10.1016/j.earscirev.2014.01.005

Kumar R, Aggarwal RK, Sharma JD, et al. (2015) Comparison of regression and artificial neural network models for estimation of global solar radiations. Renewable and Sustainable Energy Reviews 52: 1294-1299. https://doi.org/10.13140/RG.2.1.4454.5762

Laliberte AS, Fredrickson EL, Rango A (2007) Combining decision trees with hierarchical object-oriented image analysis for mapping arid rangelands. Photogrammetric Engineering and Remote Sensing 73(2): 197-207. https://doi.org/10.14358/PERS.73.2.197

Laurin GV, Chen Q, Lindsell JA, et al. (2014) Above ground biomass estimation in an African tropical forest with lidar and hyperspectral data. ISPRS Journal of Photogrammetry and Remote Sensing 89(26): 49-58. https://doi.org/10.1016/j.isprsjprs.2014.01.001

Laurin GV, Puletti N, Chen Q, et al. (2016) Above ground biomass and tree species richness estimation with airborne lidar in tropical Ghana forests. International Journal of Applied Earth Observation and Geoinformation 52: 371-379. https://doi.org/10.1016/j.jag.2016.07.008

Liu CC, Liu YG, Guo K, et al. (2016a) Aboveground carbon stock, allocation and sequestration potential during vegetation recovery in the karst region of southwestern China: A case study at a watershed scale. Agriculture, Ecosystems and Environment 235: 91-100. https://doi.org/10.1016/j.agee.2016.10.003

Liu CC, Wei YF, Liu YG, et al. (2009) Biomass of canopy and shrub layers of karst forests in Puding, Guizhou, China. Chinese Journal of Plant Ecology 33(4): 698-705. (In Chinese) https://doi.org/10.3773/j.issn.1005-264x.2009.04.008

Liu LB, Wu YY, Hu G, et al. (2016b) Biomass of karst evergreen and deciduous broad-leaved mixed forest in central Guizhou province, southwestern China: a comprehensive inventory of a 2 ha plot. Silva Fennica 50(3): 1492. https://doi.org/10.14214/sf.1492

Liu YG, Liu CC, Wang SJ, et al. (2013) Organic carbon storage in four ecosystem types in the karst region of southwestern China. Plos One 8(2): e56443. https://doi.org/10.1371/journal.pone.0106876

Lu DS (2006) The potential and challenge of remote sensing-based biomass estimation. International Journal of Remote Sensing. 27(7): 1297-1328. https://doi.org/10.1080/01431160500486732

Maack J, Kattenborn T, Fassnacht FE, et al. (2015) Modeling forest biomass using Very-High-Resolution data - Combining textural, spectral and photogrammetric predictors derived from space borne stereo images. European Journal of Remote Sensing 48(1): 245-261. http://dx.doi.org/10.5721/EuJRS20154814

Ma J, Xiao XM, Qin YW, et al. (2017) Estimating aboveground biomass of broadleaf, needle leaf, and mixed forests in Northeastern China through analysis of 25-m ALOS/PALSAR mosaic data. Forest Ecology and Management 389(1): 199-210. https://doi.org/10.1016/j.foreco.2016.12.020

Main-Knorn M, Cohen WB, Kennedy RE, et al. (2013) Monitoring coniferous forest biomass change using a Landsat trajectory-based approach. Remote Sensing of Environment 139(4): 277-290. https://doi.org/10.1016/j.rse.2013.08.010

Menlik T, Özdemir MB, Kirmaci V (2010) Determination of freeze-drying behaviors of apples by artificial neural network. Expert Systems with Applications 37(12): 7669-7677. https://doi.org/ 10.1016/j.eswa.2010.04.075

Montesano PM, Cook BD, Sun G, et al. (2013) Achieving accuracy requirements for forest biomass mapping: a space borne data fusion method for estimating forest biomass and lidar sampling error. Remote Sensing of Environment 130: 153-170. https://doi.org/10.1016/j.rse.2012.11.016

Mutanga O, Adam E, Cho MA (2012) High density biomass estimation for wetland vegetation using WorldView-2 imagery and random forest regression algorithm. International Journal of Applied Earth Observations and Geoinformation 18(1): 399-406. https://doi.org/10.1016/j.jag.2012.03.012

Muukkonen P, Heiskanen J (2005) Estimating biomass for boreal forests using ASTER satellite data combined with stand wise forest inventory data. Remote Sensing of Environment 99(4): 434-447. https://doi.org/10.1016/j.rse.2005.09.011

Özçeliǩ, R, Diamantopoulou MJ, Brooks JR, et al. (2010) Estimating tree bole volume using artificial neural network models for four species in Turkey. Journal of Environmental Management 91(3): 742-753.
https://doi.org/10.1016/j.jenvman.2009.10.002

Peña-Barragán JM, Ngugi MK, Plant RE, et al. (2011) Object-based crop identification using multiple vegetation indices, textural features and crop phenology. Remote Sensing of Environment 115(6): 1301-1316.
https://doi.org/10.1016/j.rse.2011.01.009

Powell SL, Cohen WB, Healey SP, et al. (2010) Quantification of live aboveground forest biomass dynamics with Landsat time-series and field inventory data: A comparison of empirical modeling approaches. Remote Sensing of Environment 114(5): 1053-1068. https://doi.org/10.1016/j.rse.2009.12.018

Pradhan B, Saro L (2010) Landslide susceptibility assessment and factor effect analysis: backpropagation artificial neural networks and their comparison with frequency ratio and bivariate logistic regression modelling. Environmental Modelling and Software 25(6): 747-759.
https://doi.org/10.1016/j.envsoft.2009.10.016

Quan XW, He BB, Yebra M, et al. (2017) A radiative transfer model-based method for the estimation of grassland aboveground biomass. International Journal of Applied Earth Observation and Geoinformation. 54: 159-168.
https://doi.org/10.1016/j.jag. 2016.10.002

Sedano F, Gómez D, Gong P, et al. (2008) Tree density estimation in a tropical woodland ecosystem with multiangular MISR and MODIS data. Remote Sensing of Environment 112(5): 2523-2537.
https://doi.org/10.1016/j.rse.2007.11.009

Shu GN, Kanninen M, Atyi RE, et al. (2014) Assessment and prediction of above-ground biomass in selectively logged forest concessions using field measurements and remote sensing data: Case study in South East Cameroon. Forest Ecology and Management 329(1): 177-185.
https://doi.org/10.1016/j.foreco.2014.06.018

Soenen SA, Peddle DR, Hall RJ, et al. (2010) Estimating aboveground forest biomass from canopy reflectance model inversion in mountainous terrain. Remote Sensing of Environment 114(7): 1325-1337.
https://doi.org/10.1016/j.rse. 2009.12.012

Stagakis S, Markos N, Sykioti O, et al. (2010) Monitoring canopy biophysical and biochemical parameters in ecosystem scale using satellite hyperspectral imagery: an application on a *Phlomis fruticosa* Mediterranean ecosystem using multiangular CHRIS/PROBA observations. Remote Sensing of Environment 114(5): 977-994.
https://doi.org/10.1016/j.rse.2009.12.006

Temesgen H, Affleck D, Poudel K, et al. (2015) A review of the challenges and opportunities in estimating above ground forest biomass using tree-level models. Scandinavian Journal of Forest Research 30(4): 326-335.
https://doi.org/10.1080/02827581. 2015.1012114

Tian X, Su ZB, Chen EX, et al. (2012) Estimation of forest above-ground biomass using multi-parameter remote sensing data over a cold and arid area. International Journal of Applied Earth Observation and Geoinformation 14(1): 160-168.
https://doi.org/10.1016/j.jag.2011.09.010

Tiryaki S, Aydın A (2014) An artificial neural network model for predicting compression strength of heat treated woods and comparison with a multiple linear regression model. Construction and Building Materials 62(2): 102-108.
https://doi.org/10.1016/j.conbuildmat.2014.03.041

Vahedi AA (2016) Artificial neural network application in comparison with modeling allometric equations for predicting above-ground biomass in the Hyrcanian mixed-beech forests of Iran. Biomass and Bioenergy 88: 66-76.
https://doi.org/10.1016/j.biombioe.2016.03.020

Wang C, Nie S, Xi XH, et al. (2017) Estimating the biomass of maize with hyperspectral and LiDAR data. Remote Sensing 9(1): 11. https://doi.org/10.3390/rs9010011

Wang LA, Zhou XD, Zhu XK, et al. (2016) Estimation of biomass in wheat using random forest regression algorithm and remote sensing data. The Crop Journal 4(3): 212-219.
https://doi.org/10.1016/j.cj.2016.01.008

Wu ZY (1980) Vegetation of China. Science Press, Beijing, China. (In Chinese).

Xie YC, Sha ZY, Yu M, et al. (2009) A comparison of two models with Landsat data for estimating above ground grassland biomass in Inner Mongolia, China. Ecological Modelling 220(15): 1810-1818.
https://doi.org/10.1016/j.ecolmodel.2009.04.025

Zeng SB, Jiang YJ, Liu ZH (2016) Assessment of climate impacts on the karst-related carbon sink in SW China using MPD and GIS. Global and Planetary Change 144: 171-181.
https://doi.org/10.1016/j.gloplacha.2016.07.015

Zheng DL, Rademacher J, Chen JQ, et al. (2004) Estimating aboveground biomass using Landsat 7 ETM+ data across a managed landscape in northern Wisconsin, USA. Remote Sensing of Environment 93(3): 402-411.
https://doi.org/10.1016/j.rse.2004.08.008

Zhang SY, Bai XY, Wang SJ, et al. (2015) Spatial distribution patterns and the evolution process of carbon storage in a typical karst canyon area. Journal of Resources and Ecology 6(4): 199-207.
https://doi.org/10.5814/j.issn.1674-764x.2015.04.002

Zhang Z, Tian X, Chen ER, et al. (2011) Review of methods on estimating forest above ground biomass. Journal of Beijing Forestry University 33(5): 144-150. (In Chinese)
https://doi.org/10.13332/j.1000-1522.2011.05.026

Zheng G, Chen JM, Tian QJ, et al. (2007) Combining remote sensing imagery and forest age inventory for biomass mapping. Journal of Environmental Management 85(3): 616-623.
https://doi.org/10.1016/j.jenvman.2006.07.015

Zhou XN, Lai AH, Zhou CJ, et al. (2015) Advances in ecological logging of mountain forest. Journal of Forest and Environment 27(2): 180-185. (In Chinese)
https://doi.org/10.13324/j.cnki.jfcf.2015.02.016

Zhu SQ, Wei LM, Chen ZR, et al. (1995) A preliminary study on biomass components of karst forest in Maolan of Guizhou Province, China. Acta hytoecologica Sinica 19(4): 358-367. (In Chinese)

Zhu YH, Liu K, Liu L, et al. (2015) Retrieval of mangrove aboveground biomass at the individual species level with WorldView-2 Images. Remote Sensing 7(9): 12192-12214.
https://doi.org/10.3390/rs70912192

Zolkos SG, Goetz SJ, Dubayah R (2013) A meta-analysis of terrestrial aboveground biomass estimation using lidar remote sensing. Remote Sensing of Environment 128(1): 289-298. https://doi.org/10.1016/j.rse.2012.10.017